Ferrous iron-dependent drug delivery enables controlled and selective release of therapeutic agents in vivo

Edgar Deu[a,1], Ingrid T. Chen[b], Erica M. W. Lauterwasser[b], Juan Valderramos[a], Hao Li[a], Laura E. Edgington[a], Adam R. Renslo[b,2], and Matthew Bogyo[a,c,2]

Departments of [a]Pathology and [c]Microbiology and Immunology, Stanford School of Medicine, Stanford, CA 94305; and [b]Department of Pharmaceutical Chemistry, Small Molecule Discovery Center, University of California, San Francisco, CA 94158

Edited* by Robert M. Stroud, University of California, San Francisco, California, and approved October 1, 2013 (received for review July 8, 2013)

The precise targeting of cytotoxic agents to specific cell types or cellular compartments is of significant interest in medicine, with particular relevance for infectious diseases and cancer. Here, we describe a method to exploit aberrant levels of mobile ferrous iron (Fe^{II}) for selective drug delivery in vivo. This approach makes use of a 1,2,4-trioxolane moiety, which serves as an Fe^{II}-sensitive "trigger," making drug release contingent on Fe^{II}-promoted trioxolane fragmentation. We demonstrate in vivo validation of this approach with the *Plasmodium berghei* model of murine malaria. Malaria parasites produce high concentrations of mobile ferrous iron as a consequence of their catabolism of host hemoglobin in the infected erythrocyte. Using activity-based probes, we successfully demonstrate the Fe^{II}-dependent and parasite-selective delivery of a potent dipeptidyl aminopeptidase inhibitor. We find that delivery of the compound in its Fe^{II}-targeted form leads to more sustained target inhibition with greatly reduced off-target inhibition of mammalian cathepsins. This selective drug delivery translates into improved efficacy and tolerability. These findings demonstrate the utility of a purely chemical means to achieve selective drug targeting in vivo. This approach may find useful application in parasitic infections and more broadly in any disease state characterized by aberrant production of reactive ferrous iron.

iron-mediated delivery | targeted prodrugs | dipeptidyl peptidase | combination therapy

The biological pathways underlying iron homeostasis are complex (1, 2), and their dysregulation is involved in a variety of pathologies, including cancer (2–5). Most iron in the body is present in the ferric (Fe^{III}) form, including Fe^{III} bound to its intercellular transporter transferrin and in the Fe^{III} ferritin that comprises the major iron stores of the cell. Ferrous iron is produced transiently upon release of iron from endosomes and on the way to storage as Fe^{III} ferritin, but evidence suggests that divalent metal transport proteins are likely involved (6, 7). The formation of unbound and reactive forms of ferrous iron is usually associated with disease pathology (1, 5). For example, mobile ferrous iron is produced in large quantities during the symptomatic stage of malaria. Upon invasion of red blood cells (RBCs), *Plasmodium* parasites transport hemoglobin to an acidic organelle called the digestive vacuole (DV) where the protein is degraded by a number of proteases (8). Ferrous iron heme is a toxic by-product of this process that the parasite subsequently converts into hemozoin, an inert biocrystalline material that contains oxidized heme (Fe^{III}). Although this process mitigates heme toxicity, Fe^{II} concentrations in infected red blood cells (iRBCs) are believed to be much higher than those found in serum and healthy tissues (9, 10).

Combination therapy involving artemisinin analogs represents the current standard of care in treating uncomplicated malaria. The antimalarial action of artemisinins and the newer 1,2,4-trioxolane drugs arterolane (11, 12) and OZ439 (13) is thought to involve initial Fe^{II}-promoted Fenton-type cleavage of the peroxide bond, followed by the formation of carbon-centered radical species that mediate parasite toxicity directly, or via the formation of redox-active heme adducts (14–18). However, other peroxide-dependent mechanisms of action have been put forward (19, 20). The fact that millions of malaria patients have been successfully treated with artemisinin therapy suggests a general lack of free ferrous iron species in healthy cells and tissues. Here, we describe a drug-delivery approach based on the well-studied (17, 21) Fe^{II}-promoted fragmentation of the 1,2,4-trioxolane ring system. Using this strategy, we were able to demonstrate selective delivery of a potent protease inhibitor to parasite-infected RBCs, resulting in reduced off-target toxicity and prolonged target inhibition. This strategy appears to have great potential for selective drug delivery to cells or tissues characterized by aberrant production of free ferrous iron.

Results

Design of the Delivery System. In our prototypical drug conjugate (Fig. 1), a 1,2,4-trioxolane ring (in red) is joined via a traceless linker (green) to a drug species (blue), which is conjugated to the linker via a free amine or alcohol function. Reaction with Fe^{II} unveils a ketone function in the linker, thus allowing drug release via β-elimination reaction and decarboxylation. The traceless linker is important as it affords a scope of application encompassing any drug species bearing a reactive amine or alcohol function (found in most of the existing artemisinin partner drugs). Conceptually similar antimalarial "prodrugs" have been described by another group

Significance

Selective drug delivery to diseased tissue is a promising approach to mitigate drug-related side effects while improving efficacy. This concept has been demonstrated in the case of photodynamic therapy, where activation of cytotoxic drugs at the tumor site provides a clear advantage compared with traditional chemotherapy. Here, we exploit the aberrantly high levels of mobile ferrous iron produced during the blood stage of malaria to selectively deliver a drug species to the parasite. The result is improved on-target vs. off-target action of the drug species and greater drug tolerability and efficacy. This approach should be applicable to other disease states associated with aberrant levels of ferrous iron.

Author contributions: E.D., I.T.C., E.M.W.L., H.L., L.E.E., A.R.R., and M.B. designed research; E.D., I.T.C., E.M.W.L., J.V., H.L., and L.E.E. performed research; E.D., I.T.C., E.M.W.L., J.V., H.L., L.E.E., A.R.R., and M.B. analyzed data; and E.D., A.R.R., and M.B. wrote the paper.

The authors declare no conflict of interest.

*This Direct Submission article had a prearranged editor.

[1]Present address: Division of Parasitology, Medical Research Council National Institute for Medical Research, The Ridgeway, Mill Hill, London NW7 1AA, United Kingdom.

[2]To whom correspondence may be addressed. E-mail: mbogyo@stanford.edu or adam.renslo@ucsf.edu.

This article contains supporting information online at www.pnas.org/lookup/suppl/doi:10.1073/pnas.1312782110/-/DCSupplemental.

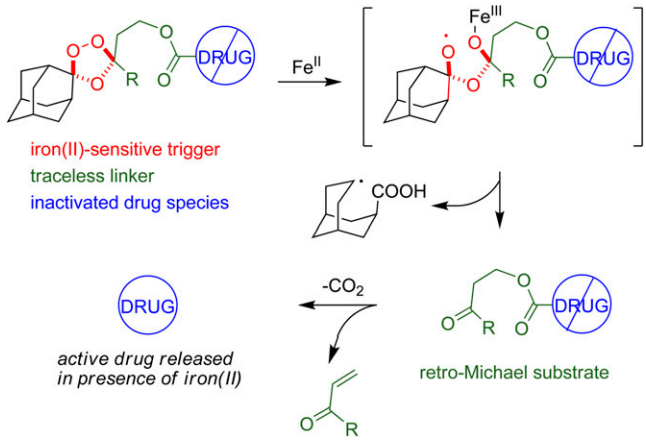

Fig. 1. Chemical processes underlying Fe^{II}-mediated drug delivery. Ferrous iron-dependent drug delivery is realized by conjugation of an Fe^{II}-reactive 1,2,4-trioxolane ring (red) to a drug species (blue) via traceless linker (green). Upon Fe^{II}-promoted cleavage of the peroxide bond, a fragmentation reaction occurs to produce a retro-Micheal substrate (green/blue), which undergoes spontaneous β-elimination to release the free drug species. Drug species can be conjugated via an amine or alcohol function, potentially allowing the intrinsic bioactivity (and/or toxicity) of the drug species to be blocked before Fe^{II}-dependent release at the desired site of action.

(22); however, those require drug conjugation via a carbonyl function, greatly limiting potential applications.

To validate our approach in parasites, we used a potent and irreversible inhibitor of the parasite cysteine protease dipeptidyl aminopeptidase 1 (DPAP1) (23–25) as our "drug" species. Several factors drove the selection of the DPAP inhibitor ML4118S (24) (herein denoted ML) (Fig. 2) for in vitro and in vivo studies. First, DPAP1 is highly expressed in blood-stage parasites and is localized to the parasite DV where it catalyzes the final stages of hemoglobin degradation (23). Thus, reactive Fe^{II} is present in the DV, and the desired release of free ML in this compartment can be detected with an activity-based probe (ABP) for DPAP activity (24, 25). Secondly, the free amino group in ML is essential as it serves to mimic the N terminus of DPAP substrates. Accordingly, ML analogs and controls in which the amino group is blocked (e.g., TRX-ML, DXL-ML) (Fig. 3) are devoid of DPAP1 inhibitory effects (24). Finally, ML is a potent inhibitor of mammalian cathepsin C, thereby providing a surrogate in vivo biomarker of undesired ML release outside of parasites.

In preliminary in vitro studies described elsewhere, we demonstrated that trioxolane conjugates undergo the desired fragmentation chemistry in vitro and can release a falcipain (26) or DPAP1 (27) inhibitor inside intraerythrocytic *Plasmodium falciparum* parasites. For example, using an activity-based probe (ABP) to follow DPAP1 inhibition over time, we calculated that ML is released from TRX-ML in live parasites with a $t_{1/2}$ of 1.5 h (27). For the current study, we synthesized additional control compounds to better tease apart the in vivo behavior of ML and TRX-ML (Fig. 3 and Fig. S1). We prepared TRX as a control for trioxolane-mediated effects of TRX-ML. The compound DXL-ML is a close structural mimic of TRX-ML that is nonreactive with Fe^{II} and therefore controls for non Fe^{II}-dependent (e.g., proteolytic) drug release from TRX-ML. We also synthesized pML (Fig. 3), the intermediate produced from TRX-ML following trioxolane activation but before β-elimination and release of free ML (Fig. 1). Finally, to better understand the dual pharmacology exhibited by TRX-ML, we synthesized an inactive (mock) form of ML (mML) as well as a mock form of TRX-ML (TRX-mML) (Figs. 2 and 3).

In Vitro Characterization of TRX-ML and Control Compounds. We first characterized the inhibitory and antimalarial properties of all test compounds and controls by measuring inhibitory potency against DPAP1 in *P. falciparum* lysates using either a competition assay involving the DPAP-selective ABP FY01 (24, 28) or a fluorogenic substrate that is highly specific for DPAP1 (29) (Table 1). As anticipated, only ML is a potent inhibitor of DPAP1. We then determined the in vitro antimalarial activity of the compounds in D10 *P. falciparum* parasites (Fig. 4). These studies revealed that TRX-ML is as potent as ML, and twofold more potent than TRX or TRX-mML (Table 1). The improved potency of TRX-ML compared with TRX-mML might be due to release of ML from TRX-ML, which is consistent with our earlier studies (27). Importantly, the dioxolane control DXL-ML is ∼1,000-fold less potent than TRX-ML, indicating that no significant amount of ML is released from DXL-ML in vitro. Similarly, mock inhibitor mML exhibits ∼1,000-fold weaker antimalarial activity than ML.

Iron-Mediated Release of ML from TRX-ML Sustains DPAP1 Inhibition in Vivo. We next monitored the release of ML from TRX-ML in vivo by following DPAP1 activity in *Plasmodium berghei*-infected mice. We accomplished this analysis by using FY01 (Fig. 5*A*), a fluorescent and cell-permeable ABP that selectively labels DPAPs (28). We found that FY01 can reliably detect DPAP1 activity in as little as 10 μL of infected blood collected from mice with a high level of parasitemia (20–40%). We used this assay to measure levels of DPAP1 activity over time in mice treated with a single dose of TRX-ML, or roughly equimolar doses of ML, TRX, DXL-ML, pML, or vehicle (Fig. 5*B* and Fig. S2). To quantify DPAP1 activity across samples, we corrected the fluorescence intensity of FY01-labeled protein based on the amount of parasite protein in each sample. We then normalized DPAP1 activity to the initial activity measured in each mouse and to the average activity values measured in vehicle-treated mice at each time point (Fig. 5*C*).

Analysis of blood samples from mice that were administered ML or the Fe^{II}-targeted form TRX-ML revealed rapid ablation of DPAP1 activity, with TRX-ML (but not ML) sustaining inhibition out to the final 24-h time point. Thus, administration of ML in the Fe^{II}-targeted form more effectively sustains DPAP1 inhibition over time. Significantly, mice dosed with dioxolane control DXL-ML showed DPAP1 activity comparable with vehicle-treated controls. This result confirms the stability of the carbamate linkage and strongly suggests that ML release from TRX-ML is Fe^{II}-dependent. As expected, administration of TRX to infected mice had no significant effect on DPAP1 inhibition. Administration of the intermediate product pML produced an initial reduction in DPAP1 activity comparable with TRX-ML or ML, but this effect was followed by a rapid recovery of DPAP1 activity, starting at 2 h with full recovery by 18 h. This effect might be due to a different metabolic and/or in vivo clearance profile for pML compared with TRX-ML or ML. Whatever the cause, the very different DPAP1 activity profiles observed in the TRX-ML and pML treatment arms (Fig. 5*C*) imply that TRX-ML activation occurs in parasites.

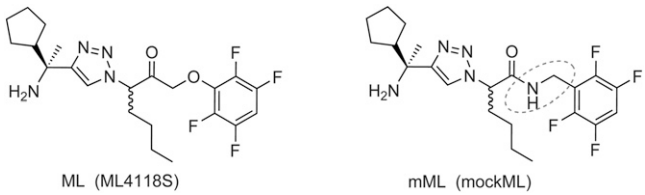

Fig. 2. Structures of ML and mML. Chemical structure of the irreversible DPAP1 inhibitor ML (ML4118S). The free amino group of ML is the site of conjugation into targeted form TRX-ML. This amine function is essential for the inhibitory effects of ML against DPAPs so conjugation at this site effectively ablates protease inhibitor activity. The inhibitor mML is a mock form of ML that is nonelectrophilic and thus unreactive with cysteine proteases.

MEDICAL SCIENCES

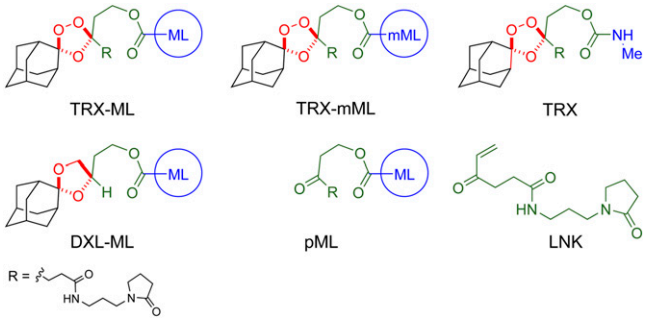

Fig. 3. Structures of the prototype TRX-ML and control compounds. Structures of trioxolane conjugates TRX-ML, TRX-mML, DXL-ML, TRX, pML, and LNK. The drug species are shown in blue and are conjugated to the linker (green) via carbamate functions (for full chemical structures, see Fig. S1). TRX-mML is a mock form of TRX-ML bearing the inactivated DPAP1 inhibitor mML. DXL-ML is a nonperoxidic analog of TRX-ML containing a dioxolane ring that is nonreactive with iron. TRX is a trioxolane control, and pML is the intermediate formed from TRX-ML following activation by Fe^{II} but before elimination of free ML. LNK is the linker by-product formed from TRX-ML following activation and release of ML.

TRX-ML Releases ML in iRBCs but Not in Peripheral Organs. We next investigated the specificity of release by monitoring ML-derived effects in peripheral organs. Because ML has some activity against host cathepsin C (CatC), the undesired release of free ML outside parasites can be detected by evaluating CatC activity in the organs of treated mice. Therefore, we treated *P. berghei*-infected mice at low parasitemia (1–3%) with 40 mg/kg TRX-ML or equimolar concentrations of ML, DXL-ML, or TRX. Eight hours after treatment, mice were euthanized, perfused, and dissected. Collected organs (heart, lung, liver, spleen, pancreas, and kidney) were then lysed and probed for residual CatC activity using FY01 (Fig. 6*A*). As expected, CatC activity was not affected in mice treated with either TRX or DXL-ML. In contrast, treatment with ML resulted in a 60–95% reduction in CatC activity depending on the organ, suggesting broad systemic distribution of the nontargeted drug species (Fig. 6). Importantly, administration of the targeted form TRX-ML produced reduced inhibition of CatC activity as compared to direct administration of ML, especially in organs that have high endogenous CatC levels such as the liver or spleen (Fig. 6 *A* and *B*). Although TRX-ML produced some reduction of CatC activity in tissues such as heart and pancreas with low endogenous levels of CatC activity, this inhibition was less pronounced with targeted TRX-ML than with untargeted ML. This result is particularly significant given that TRX-ML was more effective than ML at inhibiting the desired target DPAP1 in vivo (Fig. 5).

The inhibition of CatC in TRX-ML–treated mice could result from (*i*) partial activation of TRX-ML in serum by mobile Fe^{II} released from ruptured iRBCs, (*ii*) chemical and/or biochemical instability of the TRX-ML molecule itself, (*iii*) activation of TRX-ML by endogenous levels of Fe^{II} in host tissues, or (*iv*) diffusion of free, unreacted ML from iRBC into systemic circulation. We considered that the first and last possibilities should be dependent on parasite load because higher parasitemia should mean greater release of free ML and Fe^{II} into serum. However, we found that the level of CatC inhibition in TRX-ML-treated mice was similar regardless of whether parasitemia was low (1–3%) (Fig. 6*B*) or high (30–50%) (Fig. 6*C* and Fig. S3). The possibility of chemical/biochemical instability, although difficult to rule out absolutely, seems unlikely given that the close analog DXL-ML showed no effects on systemic CatC inhibition. Therefore, the small amount of ML released into systemic circulation likely diffused out of iRBCs, or was released from TRX-ML by endogenous Fe^{II} in host tissues. The amount of ML released by these mechanisms is apparently small, but still sufficient to inhibit CatC in tissues with low endogenous levels of this protease (Fig. S4). We also evaluated the inhibition of other mammalian cathepsins in treated mice using a broad-spectrum cathepsin ABP DCG-04 (Fig. S3). Mice administered ML had decreased Cat B, X, and L activities in various tissues whereas mice treated with TRX-ML or the control DXL-ML had activities similar to vehicle-treated controls (Figs. S3, S5, and S6). As before, the magnitude of these off-target effects was independent of parasite load. Overall, these results indicate that release of ML from TRX-ML in vivo occurs preferentially in parasites, resulting in a more sustained effect on DPAP1 inhibition over time and a significant reduction in off-target effects.

Targeted Delivery of ML from TRX-ML Improves Efficacy and Tolerability. Previously, we reported that intraperitoneal (i.p.) administration of ML to *P. berghei*-infected mice over two consecutive days decreased parasite load by 80% but produced systemic toxicity (24). We therefore sought to determine whether administration of ML in the Fe^{II}-targeted form would mitigate toxicity by reducing systemic exposure to free ML. We chose to perform proof-of-concept studies in mice bearing a high parasite load (10–20% parasitemia), thereby setting an intentionally high bar for achieving cure. Significantly, i.p. administration of TRX-ML at 40 $mg \cdot kg^{-1} \cdot day^{-1}$ for 3 d was well-tolerated, with no apparent signs of systemic toxicity. Moreover, treatment with TRX-ML decreased parasitemia below detectable levels after the second dose and effectively cured the infection (Fig. 7*A*). Some recrudescence was observed on the third and fourth week following treatment, but parasitemia remained low (< 3%) and mice were able to clear the infection without any additional treatment. The apparent lack of systemic toxicity with TRX-ML is fully consistent with parasite-selective delivery of ML from TRX-ML, as demonstrated in the in vivo kinetic studies detailed above.

We also performed studies to define the relative contributions of the trioxolane and ML components on the in vivo behavior of TRX-ML. Administration of the trioxolane control TRX at a dose equivalent (equimolar) to TRX-ML decreased parasite load initially, but parasitemia quickly increased and survival was not improved over vehicle-treated controls (Fig. 7*A*). Interestingly, dosing mice with ML alone, or a combination of TRX and ML, was wholly ineffective (Fig. 7*B*), failing to reproduce even the transient effect on parasitemia observed with TRX alone (Fig. 7*A*). All mice treated in these latter experiments showed signs of ML-mediated toxicity and were euthanized 24 h after the last treatment. Of the compounds studied, TRX-ML clearly exhibited the best combination of efficacy and tolerability and was clearly superior to TRX and ML, whether given alone or in combination. Administration of DXL-ML to infected mice had no effect on parasitemia or survival, as expected.

To further probe the role of ML in the antimalarial efficacy of TRX-ML, we prepared mML (Fig. 2), a mock form of ML that can no longer inhibit DPAP1 (Table 1). Mice were dosed for 3 d with either TRX-ML or TRX-mML (the Fe^{II}-targeted form of mML). The expectation was that TRX-ML, bearing a competent DPAP1 inhibitor, would exhibit superior efficacy to TRX-mML,

Table 1. In vitro antimalarial activity of test compounds

Compound	*Pf*DPAP1 IC_{50}, nM	*P.f.* EC_{50}, nM
TRX-ML	~10,000*,†	4.9 ± 0.4
ML	70 ± 13*,†/19 ± 1‡,§	5.2 ± 0.4
TRX	>10,000*	9.8 ± 0.3
DXL-ML	>10,000*	2,800 ± 4,000
TRX-mML	>10,000‡	8.9 ± 0.3
mML	>10,000‡	3,060 ± 4,300
LNK	>10,000*,†	>10,000†

*Pf*DPAP1, *P. falciparum*; *P.f.*, *Plasmodium falciparum*.
*IC_{50} values obtained using competition assays with a DPAP1 ABP.
†Data from ref. 27. ± indicates SD.
‡IC_{50} values obtained using competition assays with a fluorogenic substrate.
§Data from ref. 24. ± indicates SD.

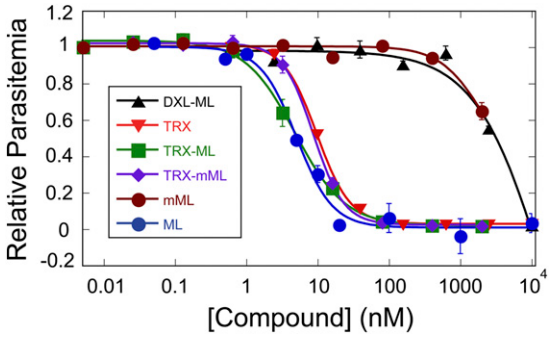

Fig. 4. Effect of test compounds on parasite replication. A synchronous culture of D10 *P. falciparum* parasite at ring stage and 2% parasitemia was treated with different concentrations of the indicated compounds. After 80 h, parasitemia was quantified by flow cytometry. Each dose–response was performed in triplicate. EC_{50} values are reported in Table 1. Bars represent SEs.

which confers only the trioxolane-based effect. Surprisingly, TRX-ML and TRX-mML had almost indistinguishable effects on parasitemia over the course of the experiment (Fig. 7*C*). The superior efficacy of TRX-mML compared with the original trioxolane control TRX (Fig. 7 *A* and *C*) suggests that appending mML or ML to the trioxolane moiety produces a favorable effect on the in vivo pharmacokinetic and/or pharmacodynamic (PK/PD) profile of TRX-mML or TRX-ML, respectively. Therefore, it is not possible to determine the additional benefit of ML release in vivo using controls such as TRX-mML. Despite this limitation, the in vivo kinetic and efficacy studies described herein clearly demonstrate the successful Fe^{II}-dependent release of ML from TRX-ML in vivo.

Discussion

Drug-targeting strategies involving conjugation to antibodies or essential nutrients (e.g., folate) continue to be actively investigated and optimized. Other drug-targeting approaches under clinical investigation include tumor-activated prodrugs (30) and siderophore-bearing β-lactams that exploit bacterial iron acquisition mechanisms. Herein, we propose that the production of mobile, unbound ferrous iron represents another characteristic of certain disease states that can potentially be exploited for selective drug targeting. Previously, we validated this notion in cultured *P. falciparum* parasites, demonstrating that a protease inhibitor could be masked with an Fe^{II}-reactive linker, and then released within parasites (26, 27). Now, we have successfully demonstrated this drug delivery approach in the mouse, revealing the benefits of Fe^{II}-dependent drug delivery at the level of the whole animal.

In the current study, we observed superior efficacy and tolerability with TRX-ML compared with ML or a combination of TRX and ML. Although these findings are consistent with effective drug targeting, they are by themselves too qualitative in nature to firmly validate the approach. Accordingly, the use of ABPs in concert with carefully designed controls such as DXL-ML, pML, and TRX affords a powerful, semiquantitative approach to study the complex in vivo behavior of a molecule like TRX-ML. Thus, the failure of control DXL-ML to liberate active ML demonstrates that in vivo release is peroxide-dependent and, by extension, Fe^{II}-dependent. Likewise, the improved tolerability of TRX-ML compared with ML can be understood in light of the reduced inhibition of mammalian cathepsins with TRX-ML treatment, as revealed by analysis of mouse tissues using ABPs. The improved target selectivity of TRX-ML in vivo also indicates that Fe^{II}-promoted activation occurs selectively in parasites. Finally, the studies with pML provide a second line of evidence that TRX-ML activation occurs within parasites (Fig. 5*C*).

In addition to validating the concept of Fe^{II}-targeted delivery, our studies also reveal a deficiency in prototypical molecules such as TRX-ML. We observed some systemic release of free ML in TRX-ML–treated mice (Fig. 6), indicating less than perfect drug targeting. This effect seems not to be related to parasite load, suggesting instead activation by endogenous levels of ferrous iron in some tissues. Other possibilities such as chemical instability or escape of free ML from iRBC seem less likely based on our experimental results, but are not possible to exclude. Whatever the cause, it is likely that improved selectivity can be achieved through further optimization of the 1,2,4-trioxolane moiety. It is well-known from studies of antimalarial 1,2,4-trioxolanes that rates of Fe^{II}-promoted fragmentation are highly sensitive to the steric environment immediately surrounding the peroxide bond (31). Our initial studies with a second generation of Fe^{II}-targeted drug conjugates suggest that structural modification of the trioxolane moiety can indeed impact the kinetics of Fe^{II} activation and stability in whole blood.

The DPAP1 inhibitor ML was selected both because its action in vivo could be readily followed with ABPs, and also because inhibition of DPAP1 by released ML was expected to offer a second beneficial antimalarial effect in vivo. DPAP1 appears to be essential in *P. falciparum* because attempts to delete the *dpap1* gene have been unsuccessful (23). We have previously shown that selective inhibition of DPAP1 is sufficient to block parasite replication both in vitro (*P. falciparum*) and in vivo (*P. berghei*) (24). We also established that sustained inhibition of DPAP1 for several hours is required to block parasite replication in vitro. Our initial in vivo studies with ML showed that treating mice at 20 mg/kg every 12 h for two consecutive days decreased parasitemia by 80% (24). Unfortunately, the toxicity associated with ML prevented the use of higher doses or longer dosing regimens. Current and previous in vivo studies of ML suggest that a 20 mg/kg dose can sustain DPAP1 inhibition if administered every 12 h (24), but that treatment every 24 h results in full recovery of DPAP1 activity between treatments

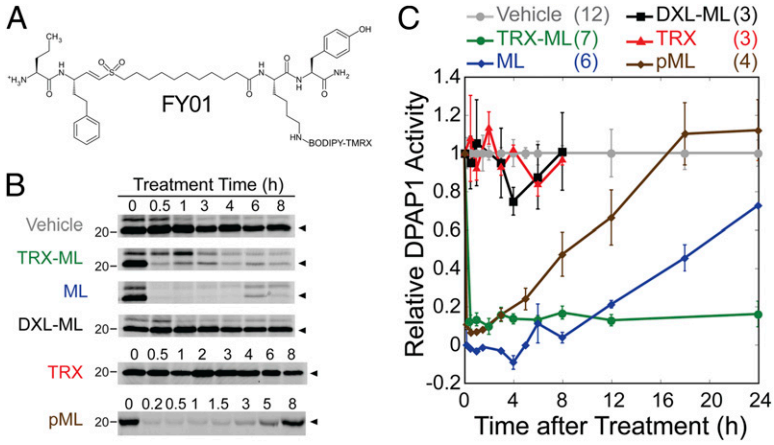

Fig. 5. Kinetics of DPAP1 inhibition in vivo. (*A*) Structure of FY01, a BODIPY-TMRX fluorescent ABP used to label DPAP activity. (*B*) Representative time course of DPAP1 inhibition after treatment with each compound. Infected mice at 20–40% parasitemia were treated with vehicle, TRX-ML (40 mg/kg), ML (20 mg/kg), DXL-ML (21 mg/kg), TRX (31 mg/kg), or pML (40 mg/kg). For each mouse, 10 μL of blood was collected from the tail vein before (t = 0 h) and at different time points after treatment. Residual DPAP1 activity was labeled with 1 μM FY01 and measured with a flat bed fluorescent scanner. The position of labeled DPAP1 is indicated with arrowheads. (*C*) DPAP1 activity progress curves in response to treatment. For each mouse, the level of DPAP1 activity was corrected based on protein loading and normalized with respect to the initial activity value. Average values relative to vehicle controls are shown. The number of mice treated with each compound is shown in parentheses. Bars represent SEs.

MEDICAL SCIENCES

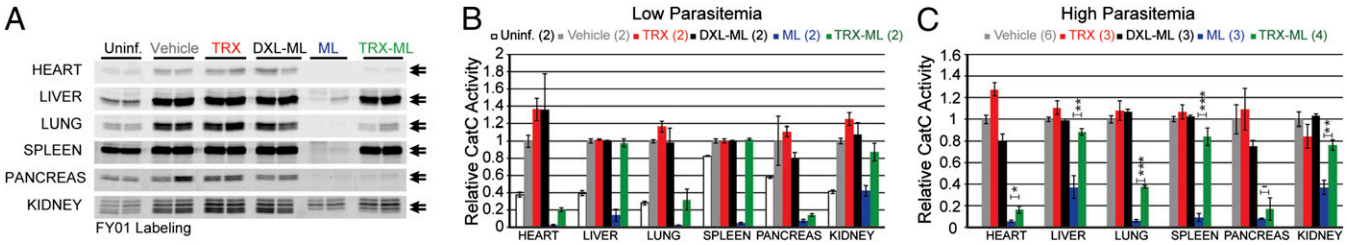

Fig. 6. Measurement of CatC inhibition in host tissues. (*A*) Inhibition of CatC in different mouse organs. Infected mice at 1–3% parasitemia were treated with 40 mg/kg TRX-ML or equimolar concentrations of TRX, DXL-ML, ML, or vehicle. Eight hours after treatment, mice were euthanized and dissected. The level of CatC activity in each organ lysate was labeled with 1 μM FY01 for 1 h and run on an SDS/PAGE gel. CatC activity was visualized using a flat bed fluorescent scanner. For comparison, the level of CatC in uninfected/untreated mice was also measured (Uninf.). The labeled CatC doublet is indicated by arrows. (*B* and *C*) Quantification of CatC activity in different organs after treatment of mice at low (1–3%) or high (20–40%) parasitemia, respectively. The number of mice treated with each compound is shown in parentheses. Bars represent SEs, and *t* test significance values between TRX-ML and ML treatment are shown (*$P < 0.05$; **$P < 0.01$; ***$P < 0.001$; -, not significant).

(Fig. 5*C*), resulting in a failure to cure infection (Fig. 7*B*). Overall, our studies with ML indicate that sustained inhibition of DPAP1 is likely required to decrease parasite burden in the *P. berghei* murine model of malaria.

The superior in vivo efficacy of TRX-ML compared with trioxolane control TRX (Fig. 7*A*) or a combination of TRX and ML (Fig. 7*B*) suggests a favorable therapeutic effect attributable to DPAP1 inhibition. The compound TRX-mML was subsequently devised as a more structurally faithful control for the trioxolane-based effects of TRX-ML. The finding that TRX-mML was just as efficacious as TRX-ML (Fig. 7*C*) was unexpected given that the parent TRX was relatively ineffective at clearing parasites. We believe the increased efficacy of TRX-mML is most likely a result of enhanced PK/PD properties that produce a more efficacious trioxolane-based effect in vivo. Unfortunately, this effect makes it impossible to discern the benefit of DPAP inhibition in the in vivo activity of TRX-ML, even though release of free ML has clearly been established via the kinetic studies described herein. Regardless of this limitation, our results demonstrate that parasite-selective delivery of ML from TRX-ML effectively eliminates the systemic toxicity observed in mice treated with ML directly.

Ferrous iron-targeted drug delivery as conceptualized herein may find favorable application in the treatment of malaria. Current artemisinin combination therapy seeks to pair a fast-acting artemisinin-based insult with the more prolonged action of a partner drug. Our data suggest that the peroxidic insult of TRX-ML is similarly fast acting, a conclusion that can be inferred from the observation that TRX-ML administration leads to maximal DPAP1 inhibition (80%) in less than 30 min, without any further decrease in activity over time. At the same time, TRX-ML treatment produces longer-lasting effects on DPAP1 inhibition than does the direct administration of either ML or its precursor pML (Fig. 5*C*). This favorable property of TRX-ML likely reflects rapid Fe^{II}-promoted formation of pML preferentially in parasites, and slower release of ML from pML via β-elimination reaction. This interpretation is also consistent with our earlier finding that reaction of TRX-ML with inorganic Fe^{II} salts leads to the formation of pML within minutes whereas release of free ML from pML requires hours (27). Thus, prototypical conjugate TRX-ML combines a fast-acting 1,2,4-trioxolane–based insult with the slow release of a partner drug, thus sustaining its effect in vivo. In principle, this approach might even be used to extend the in vivo exposure of antimalarial partner drugs with intrinsically rapid elimination profiles. The rate of β-elimination might even be fine-tuned through modification of the retro-Michael linker, as has been demonstrated recently in the context of drug release from macromolecular carriers (32, 33).

The studies described herein provide in vivo validation for the concept of ferrous iron-dependent drug delivery. This unique approach for selective drug targeting merits further investigation in the context of malaria and in other diseases of blood-feasting parasites. Such targeted agents may be particularly useful in antiparasitic prophylaxis or in mass drug administration campaigns,

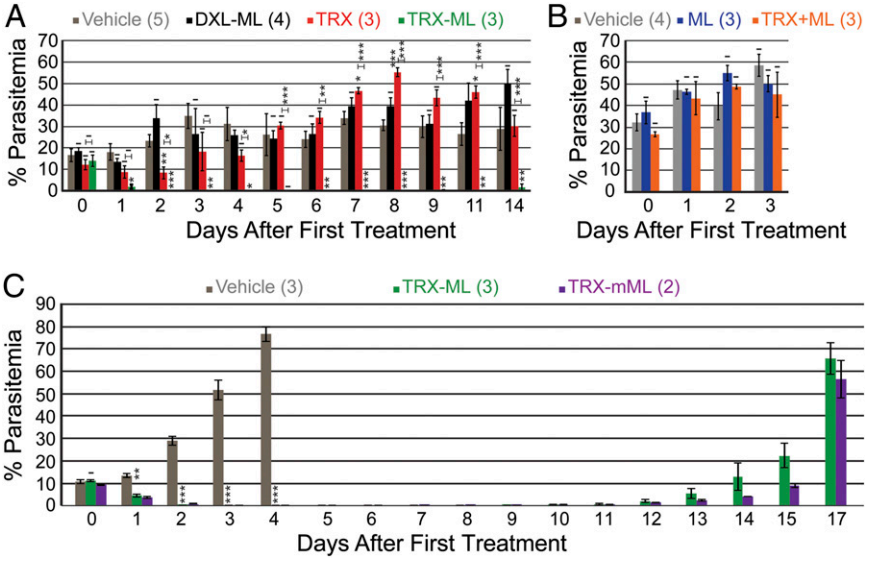

Fig. 7. In vivo efficacy studies. Mice infected with *P. berghei* parasites were treated for three consecutive days—starting on day 10 after infection—with 40 mg/kg/day of TRX-ML, or equimolar concentrations of DXL-ML (21 mg/kg/day), TRX (31 mg/kg/day), TRX-mML (40 mg/kg/day), ML (20 mg/kg/day), vehicle, or a combination of TRX and ML (TRX+ML). Parasitemia was monitored daily by Geimsa-stained thin blood smears. Values at day 0 correspond the initial parasitemia right before treatment, and those at days 1, 2, and 3 were measured 24 h after the first, second, and third treatment, respectively. (*A*), (*B*), and (*C*) correspond to three independent experiments. Bars represent SEs, and the number of mice treated with each compound is shown in parentheses. T-test significance values relative to vehicle treated mice, and between TRX and TRX-ML are shown (*$P < 0.05$ **$P < 0.01$; ***$P < 0.001$; —, not significant).

wherein an uninfected patient would not be exposed to active partner drug species. More broadly, Fe^{II}-dependent drug delivery could find application in any disease state characterized by the dysregulation of iron metabolism.

Materials and Methods

Kinetics of DPAP1 Inhibition in Vivo. All mice experiments were approved by the Stanford Administration Panel on Laboratory Animal Care and strictly followed their specific guidelines. All treatments were administered via i.p. in 45% (vol/vol) polyethylene glycol (M.W. 400), 35% (vol/vol) propylene glycol, 10% (vol/vol) ethanol, 10% DMSO, and 10% (wt/vol) 2-hydroxypropyl β-cyclodextrin. BALB/c female mice (20-24 g) were inoculated via tail vein with 10^6 *P. berghei* parasites freshly collected from an infected mice at ∼3% parasitemia. Mice were treated with different test compounds or vehicle when parasitemia reached 20–40%, usually 12 d after infection. The level of DPAP1 activity right before treatment (t_0) or at different time points afterward was measured as follows. Two 5-μL drops of blood were collected from the tail vein of infected mice and diluted in 10 μL of 2× heparin in PBS. DPAP1 activity was label for 1 h in intact cells by adding 0.4 μL of 50 μM FY01 (final concentration 1 μM). RBC and parasitophorous vacuole membranes were then lysed by adding 20 μL of 0.3% saponin in PBS and incubating the samples at 37 °C for 10 min. Parasite pellets were washed with 1 mL of PBS, collected by centrifugation, and frozen in liquid nitrogen. Once all pellets had been collected, they were diluted in 40 μL of 1× SDS/PAGE loading buffer, boiled for 10 min, and run on a 15% SDS/PAGE gel. After measurement of in-gel fluorescence using a Typhoon Scanner (GE Healthcare), gels were stained with gel code blue to determine the relative amount of *Plasmodium* protein in each sample.

The level of DPAP1 activity for each mouse was quantified as follows. ImageJ was used to quantify the intensity of DPAP1 labeling in each sample as well as the relative amount of protein stained with gel code blue. DPAP1 labeling was corrected based on protein concentration—i.e., DPAP1 labeling intensity divided by protein content—to take into consideration time-dependent changes in parasitemia throughout the experiment and experimental variation in collecting blood samples. For each mouse, DPAP1 activity was normalized to the initial value and divided by the average level of DPAP1 activity measured in vehicle-treated mice at each time point. The later normalization accounts for variation in labeling efficiency at different time points throughout the experiment.

Measurement of Host Off-Target Effects. Mice were treated with different test compounds 3 or 12 d after infection (1-3% or 20–40% parasitemia, respectively). Eight hours after treatment, mice were euthanized and perfused with PBS, and samples of heart, liver, lung, spleen, pancreas, and kidney were collected and frozen in liquid nitrogen. Organs were lysed in citrate buffer, and cathepsin activity was measured as previously described (34, 35). Briefly, 50 μg of protein lysate was labeled for 1 h at room temperature with a mixture of 1 μM FY01 and 1 μM DCG04, and run on an SDS/PAGE gel. Because FY01 and DCG04 have different fluorophores (BODIPY-TMRX and Cy5, respectively), in-gel fluorescence was scanned at two different wavelengths to differentiate between CatC activity and the labeling of the other cysteine cathepsins. The level of CatC activity and the combined or individual activity of all other cysteine cathepsins labeled were quantified using ImageJ.

In Vivo Efficacy Studies. Infected mice at 10–20% parasitemia (i.e., 10 d post-infection) were treated for three consecutive days with vehicle or equimolar concentrations of TRX-ML (40 mg/kg), TRX (21 mg/kg), DXL-ML (31 mg/kg), TRX-mML (40 mg/kg), ML (20 mg/kg), or a combination of ML (20 mg/kg) and TRX (21 mg/kg). Parasite load was monitored daily for the first 2 wk after treatment and every 3 d afterward. Parasitemia was quantified from Giemsa-stained thin blood smears as previously described (24).

Details of compound synthesis, *P. falciparum* replication assays, and in vitro DPAP1 inhibition studies are outlined in *SI Materials and Methods*.

ACKNOWLEDGMENTS. We thank Dr. Jonathan Ellman (Yale University) for providing the ML4118S compound used in these studies. This work was supported by a Burroughs Wellcome Trust New Investigators in Pathogenesis Award (to M.B.), the Bill and Melinda Gates Foundation (A.R.R. and M.B.), and National Institutes of Health Grants AI094433 (to A.R.R.) and R01-AI078947 and EB005011 (to M.B.).

1. Hentze MW, Muckenthaler MU, Galy B, Camaschella C (2010) Two to tango: Regulation of Mammalian iron metabolism. *Cell* 142(1):24–38.
2. Kwok JC, Richardson DR (2002) The iron metabolism of neoplastic cells: Alterations that facilitate proliferation? *Crit Rev Oncol Hematol* 42(1):65–78.
3. Saletta F, Kovacevic Z, Richardson DR (2011) Iron chelation: Deciphering novel molecular targets for cancer therapy. The tip of the iceberg of a web of iron-regulated molecules. *Future Med Chem* 3(16):1983–1986.
4. Efferth T, et al. (2004) Enhancement of cytotoxicity of artemisinins toward cancer cells by ferrous iron. *Free Radic Biol Med* 37(7):998–1009.
5. Toyokuni S (2009) Role of iron in carcinogenesis: Cancer as a ferrotoxic disease. *Cancer Sci* 100(1):9–16.
6. Richardson DR, Ponka P, Vyoral D (1996) Distribution of iron in reticulocytes after inhibition of heme synthesis with succinylacetone: Examination of the intermediates involved in iron metabolism. *Blood* 87(8):3477–3488.
7. Ponka P (1997) Tissue-specific regulation of iron metabolism and heme synthesis: distinct control mechanisms in erythroid cells. *Blood* 89(1):1–25.
8. Li H, Child MA, Bogyo M (2012) Proteases as regulators of pathogenesis: Examples from the Apicomplexa. *Biochim Biophys Acta* 1824(1):177–185.
9. Sullivan DJ, Jr., Gluzman IY, Russell DG, Goldberg DE (1996) On the molecular mechanism of chloroquine's antimalarial action. *Proc Natl Acad Sci USA* 93(21):11865–11870.
10. Robert A, Benoit-Vical F, Meunier B (2005) The key role of heme to trigger the antimalarial activity of trioxanes. *Coord Chem Rev* 249(17-18):1927–1936.
11. Vennerstrom JL, et al. (2004) Identification of an antimalarial synthetic trioxolane drug development candidate. *Nature* 430(7002):900–904.
12. Valecha N, et al. (2010) Arterolane, a new synthetic trioxolane for treatment of uncomplicated Plasmodium falciparum malaria: A phase II, multicenter, randomized, dose-finding clinical trial. *Clin Infect Dis* 51(6):684–691.
13. Moehrle JJ, et al. (2013) First-in-man safety and pharmacokinetics of synthetic ozonide OZ439 demonstrates an improved exposure profile relative to other peroxide antimalarials. *Br J Clin Pharmacol* 75(2):524–537.
14. Hartwig CL, et al. (2011) Investigating the antimalarial action of 1,2,4-trioxolanes with fluorescent chemical probes. *J Med Chem* 54(23):8207–8213.
15. Hartwig CL, et al. (2009) Accumulation of artemisinin trioxane derivatives within neutral lipids of Plasmodium falciparum malaria parasites is endoperoxide-dependent. *Biochem Pharmacol* 77(3):322–336.
16. Fügi MA, Wittlin S, Dong Y, Vennerstrom JL (2010) Probing the antimalarial mechanism of artemisinin and OZ277 (arterolane) with nonperoxidic isosteres and nitroxyl radicals. *Antimicrob Agents Chemother* 54(3):1042–1046.
17. Creek DJ, et al. (2008) Relationship between antimalarial activity and heme alkylation for spiro- and dispiro-1,2,4-trioxolane antimalarials. *Antimicrob Agents Chemother* 52(4):1291–1296.
18. Mercer AE, et al. (2007) Evidence for the involvement of carbon-centered radicals in the induction of apoptotic cell death by artemisinin compounds. *J Biol Chem* 282(13):9372–9382.
19. Eckstein-Ludwig U, et al. (2003) Artemisinins target the SERCA of *Plasmodium falciparum*. *Nature* 424(6951):957–961.
20. Haynes RK, et al. (2012) Interactions between artemisinins and other antimalarial drugs in relation to the cofactor model—a unifying proposal for drug action. *ChemMedChem* 7(12):2204–2226.
21. Tang Y, et al. (2005) Dispiro-1,2,4-trioxane analogues of a prototype dispiro-1,2,4-trioxolane: Mechanistic comparators for artemisinin in the context of reaction pathways with iron(II). *J Org Chem* 70(13):5103–5110.
22. O'Neill PM, et al. (2004) Design and synthesis of endoperoxide antimalarial prodrug models. *Angew Chem Int Ed Engl* 43(32):4193–4197.
23. Klemba M, Gluzman I, Goldberg DE (2004) A Plasmodium falciparum dipeptidyl aminopeptidase I participates in vacuolar hemoglobin degradation. *J Biol Chem* 279(41):43000–43007.
24. Deu E, et al. (2010) Functional studies of Plasmodium falciparum dipeptidyl aminopeptidase I using small molecule inhibitors and active site probes. *Chem Biol* 17(8):808–819.
25. Arastu-Kapur S, et al. (2008) Identification of proteases that regulate erythrocyte rupture by the malaria parasite Plasmodium falciparum. *Nat Chem Biol* 4(3):203–213.
26. Mahajan SS, Gut J, Rosenthal PJ, Renslo AR (2012) Ferrous iron-dependent delivery of therapeutic agents to the malaria parasite. *Future Med Chem* 4(18):2241–2249.
27. Mahajan SS, et al. (2011) A fragmenting hybrid approach for targeted delivery of multiple therapeutic agents to the malaria parasite. *ChemMedChem* 6(3):415–419.
28. Yuan F, Verhelst SH, Blum G, Coussens LM, Bogyo M (2006) A selective activity-based probe for the papain family cysteine protease dipeptidyl peptidase I/cathepsin C. *J Am Chem Soc* 128(17):5616–5617.
29. Deu E, Yang Z, Wang F, Klemba M, Bogyo M (2010) Use of activity-based probes to develop high throughput screening assays that can be performed in complex cell extracts. *PLoS ONE* 5(8):e11985.
30. Denny WA (2004) Tumor-activated prodrugs—a new approach to cancer therapy. *Cancer Invest* 22(4):604–619.
31. Creek DJ, et al. (2007) Iron-mediated degradation kinetics of substituted dispiro-1,2,4-trioxolane antimalarials. *J Pharm Sci* 96(11):2945–2956.
32. Santi DV, Schneider EL, Reid R, Robinson L, Ashley GW (2012) Predictable and tunable half-life extension of therapeutic agents by controlled chemical release from macromolecular conjugates. *Proc Natl Acad Sci USA* 109(16):6211–6216.
33. Ashley GW, Henise J, Reid R, Santi DV (2013) Hydrogel drug delivery system with predictable and tunable drug release and degradation rates. *Proc Natl Acad Sci USA* 110(6):2318–2323.
34. Verdoes M, et al. (2012) A nonpeptidic cathepsin S activity-based probe for non-invasive optical imaging of tumor-associated macrophages. *Chem Biol* 19(5):619–628.
35. Paulick MG, Bogyo M (2011) Development of activity-based probes for cathepsin X. *ACS Chem Biol* 6(6):563–572.

Supporting Information

Deu et al. 10.1073/pnas.1312782110

SI Materials and Methods

***P. falciparum* Replication Assay.** Replication assays using a synchronous culture of D10 *P. falciparum* parasites were performed as described before (1). Briefly, ring stage parasites at 2% parasitemia were treated with different concentrations of test compound or DMSO for 80 h, i.e., until control parasites reach schizont stage. Parasitemia was quantified by flow cytometry after fixing the cells and staining for DNA with propidium iodide. EC_{50} values were determined by fitting the parasitemia values to a dose–response curve using Kaleidagraph. All assays were performed in triplicate.

Dipeptidyl aminopeptidase 1 Inhibition Assays. Dipeptidyl aminopeptidase 1 (DPAP1) inhibition in parasite lysates was generally determined using a competition assay against FY01 (1). Parasite lysates were diluted 10-fold into acetate buffer (50 mM sodium acetate, 5 mM $MgCl_2$, and 5 mM dithiothreitol at pH 5.5) and incubated with different concentrations of test compound for 30 min, and residual DPAP1 activity was label with 1 μM FY01 for 1 h. After boiling, the samples in loading buffer and running them on a 15% SDS/PAGE gel, in-gel fluorescence was measured using a Typhoon Scanner (GE Healthcare). The level of DPAP1 activity corresponding to the doublet band labeled around 20 kDa was quantified using ImageJ. IC_{50} values were determined by fitting the data to a dose–response curve using Kaleidagraph.

The IC_{50} values for TRX-mML and mML were determined using a fluorogenic assay because these compounds were not expected to be covalent inhibitors and would therefore be outcompeted by our covalent ABP. Parasite lysates were diluted 100-fold in acetate buffer containing different concentrations of compound and 10 μM $(PR)_2$Rho, a fluorogenic substrate that is specific for DPAP1 in parasite lysates (2). No significant inhibition was observed at concentrations as high as 10 μM. This assay was performed in triplicate, and ML was used as a positive control.

Compound Synthesis and Characterization

The synthesis and characterization of ML and TRX-ML were described in refs. 1 and 3, respectively.

General Methods. ^{1}H NMR spectra were recorded on a Varian INOVA-400 400 MHz spectrometer. Chemical shifts are reported in δ units (ppm) relative to tetramethylsilane as an internal standard. Coupling constants (*J*) are reported in hertz (Hz). All reagents and solvents were purchased from Aldrich Chemical or Acros Organics and used as received unless otherwise indicated. Compound **S-1** (Fig. S7), TRX-ML, and TRX were prepared as described previously (3). Compound **S-3** (Fig. S7) was a gift of Jonathan Ellman (Yale University, New Haven, CT). Other synthetic intermediates were prepared according to literature procedures, as indicated. Air- and/or moisture-sensitive reactions were carried out under an argon atmosphere in oven-dried glassware using anhydrous solvents from commercial suppliers. Air- and/or moisture-sensitive reagents were transferred via syringe or cannula and were introduced into reaction vessels through rubber septa. Solvent removal was accomplished with a rotary evaporator at ∼10–50 Torr. Column chromatography was carried out using a Biotage SP1 flash chromatography system and silica gel cartridges from Biotage. Analytical thin layer chromatography (TLC) plates from EM Science (Silica Gel 60 F254) were used for TLC analyses. Mass analyses and compound purity were determined using Waters Micromass ZQTM, equipped with Waters 2795 Separation Module and Waters 2996 Photodiode Array Detector. Separations were carried out with an XTerra MS C18, 5μm, 4.6 × 50 mm column, at ambient temperature (unregulated) using a mobile phase of water-acetonitrile containing a constant 0.20% formic acid.

Synthesis of 2-[(3R)-3-[3-oxo-3-[3-(2-oxopyrrolidin-1-yl)propylamino]propyl]spiro[1,2,4-trioxolane-5,2′-adamantane]-3-yl]ethyl *N*-[(2S)-2-cyclopentylbut-3-yn-2-yl]carbamate (Intermediate S-4; Scheme S1). To a solution of (2S)-2-cyclopentylbut-3-yn-2-amine hydrochloride (4) (15 mg, 0.086 mmol) in dimethylformamide (DMF) (1.0 mL) was added N,N-Diisopropylethylamine (DIEA) (31 μL, 0.18 mmol), and the pale yellow solution was stirred for 5 min, at which point a solution of (4-nitrophenyl) 2-[(3R)-3-[3-oxo-3-[3-(2-oxopyrrolidin-1-yl)propylamino]propyl]spiro[1,2,4-trioxolane-5,2'-adamantane]-3-yl]ethyl carbonate (**S-1**, 48 mg, 0.080 mmol) in DMF (1.0 mL), followed by 4-Dimethylaminopyridine (DMAP) (2.0 mg, 0.016 mmol). The pale yellow solution was stirred for 18 h and then diluted with EtOAc, after which a saturated aqueous solution of $NaHCO_3$ was added. The layers were separated, and the organic layer was washed once each with a saturated aqueous solution of $NaHCO_3$, 1.0 M NaOH, and saturated aqueous NaCl. The organic layer was then dried over $MgSO_4$, filtered, and evaporated, and the crude material was purified using automated flash chromatography (3–5% MeOH/EtOAc) to obtain 37 mg of intermediate **S-4** (77%) as a glassy colorless solid. R_f 0.18 (2.5% MeOH/EtOAc). ^{1}H NMR (400 MHz, $CDCl_3$): δ 6.73 (m, 1H), 5.50 (br s, 1H), 4.18 (t, 2H, $J = 8$ Hz), 3.39 (t, 2H, $J = 8$ Hz), 3.36 (dd, 2H, $J = 4, 8$ Hz), 3.18 (m, 2H), 2.44 (t, 2H, $J = 8$ Hz), 2.32 (m, 3H), 2.18–1.16 (m, 34H). MS for $C_{33}H_{49}N_3O_7$ calc'd 599.76, found 600.3 $(M+H)^+$.

Synthesis of [3,6-dioxo-6-[3-(2-oxopyrrolidin-1-yl)propylamino]hexyl] *N*-[(1S)-1-cyclopentyl-1-[1-[2-oxo-1-(2,3,5,6-tetrafluorophenoxy)heptan-3-yl]triazol-4-yl]ethyl]carbamate (pML; Scheme S1). To a solution of intermediate **S-4** (6 mg, 0.01 mmol) and 3-azido-1-(2,3,5,6-tetrafluorophenoxy)heptan-2-one (4) (**S-2**, 5 mg, 0.016 mmol) in dichloromethane (0.4 mL) and H_2O (0.32 mL) was added $CuSO_4$ (37 μL, 0.3M in H_2O, 0.011 mmol), followed by sodium ascorbate (28 μL, 1.0 M in H_2O, 0.028 mmol). The reaction mixture was stirred vigorously and turned brown upon addition of sodium ascorbate, then yellow within minutes. After 1 h, the reaction mixture was green in color. The reaction mixture was stirred for an additional 3.5 h and then diluted with EtOAc, after which a saturated aqueous solution of $NaHCO_3$ was added. The layers were separated, and the organic layer was washed with a saturated aqueous solution of $NaHCO_3$ (1×) and saturated aqueous NaCl (1×). The organic layer was then dried over $MgSO_4$, filtered, and evaporated, and the crude material was purified using the Biotage (5–10% MeOH/CH_2Cl_2) to obtain 6 mg of pML (73%) as a viscous colorless oil. R_f 0.47 (10% MeOH/ CH_2Cl_2). ^{1}H NMR (400 MHz, $CDCl_3$): δ 7.60 (s, 1H), 6.80 (m, 2H), 5.52 (m, 2H), 4.86 (s, 2H), 4.23 (m, 2H), 3.37 (m, 4H), 3.16 (dd, 2H, $J = 4, 12$ Hz), 2.73 (m, 3H), 2.46 (t, 2H, $J = 8$ Hz), 2.39 (t, 2H, $J = 8$ Hz), 2.29 (m, 2H), 2.06 (m, 4H), 1.75 (s, 3H), 1.64 (m, 4H), 1.48–1.21 (m, 10H), 0.86 (m, 3H, $J = 4$ Hz). ^{13}C NMR (100 MHz, $CDCl_3$): δ 199.61, 176.06, 171.96, 152.46, 147.76, 121.52, 100.33 (m), 75.48, 65.85, 59.52, 56.41, 47.54, 42.09, 39.76, 38.21, 35.90, 31.11, 30.79, 30.03, 27.83, 27.40, 27.33, 26.68, 25.94, 25.85, 25.82, 22.93, 22.09, 18.14, 13.88. ^{19}F NMR (100 MHz, $CDCl_3$): δ 139.53 (m), 157.41 (m). MS for $C_{36}H_{48}F_4N_6O_7$ calc'd 752.35, found 753.2 $(M+H)^+$.

Synthesis of 2-[(3R)-3-[3-oxo-3-[3-(2-oxopyrrolidin-1-yl)propylamino]propyl]spiro[1,2,4-trioxolane-5,2′-adamantane]-3-yl]ethyl *N*-[(1S)-1-cyclopentyl-1-[1-[2-oxo-1-(2,3,5,6-tetrafluorophenoxy)heptan-3-yl]triazol-4-yl]ethyl]carbamate (TRX-ML). TRX-ML was prepared from the reaction of ML (1) with intermediate **S-1** as described previously (3). ^{1}H NMR and ^{19}F NMR spectra of this material were identical to that reported previously. A more complete ^{13}C NMR spectrum was recorded on the material used herein, and these data are provided. ^{13}C NMR (75 MHz, $CDCl_3$): δ 199.45, 175.87, 172.25, 154.64, 152.42, 147.76 (m), 144.70 (m), 141.88 (m), 138.77 (m), 136.73 (m), 121.51, 112.16, 109.65, 100.11 (m), 75.26, 65.68, 60.11, 56.14, 50.78, 48.65, 47.32, 39.59, 36.68, 36.31, 36.20, 35.67, 35.00, 34.78, 34.71, 34.58, 31.63, 31.12, 30.92, 30.62, 27.64, 27.59, 27.17, 26.75, 26.50, 26.39, 25.76, 25.70, 25.65, 21.89, 17.95, 13.69.

Synthesis of 2-azido-*N*-[(2,3,5,6-tetrafluorophenyl)methyl]hexanamide (intermediate S-5; Scheme S2). To a solution of 2-azidohexanoic acid (4) (41 mg, 0.26 mmol) in DMF (3 mL) was added 2,6-lutidine (34 μL, 0.29 mmol), and 1-[Bis(dimethylamino)methylene]-1H-1,2,3-triazolo[4,5-b]pyridinium 3-oxid hexafluorophosphate (HATU) (0.27 mmol). After 10 min of stirring, a solution of (2,3,5,6-tetrafluorophenyl)methanamine (40 mg, 0.22 mmol) in DMF (2 mL) was added, and the pale yellow reaction mixture was stirred at room temperature for 4 h, then diluted with Et_2O and washed with aqueous saturated $NaHCO_3$ and saturated aqueous NaCl. The organic extracts were dried over $MgSO_4$, filtered, and evaporated, and the crude material was purified using automated flash chromatography (12 g SiO_2, 20–50% EtOAc/hexanes) to obtain intermediate **S-5** (58 mg, 82%) as a white solid. R_f 0.53 (25% EtOAc/hexanes). ^{1}H NMR (400 MHz, $CDCl_3$): δ 7.03 (m, 1H), 6.80 (br s, 1H), 4.59 (d, 2H, J = 4 Hz), 3.99 (dd, 1H, J = 4, 8 Hz), 1.90 (m, 1H), 1.84 (m, 1H), 1.34 (m, 4H), 0.88 (t, 3H, J = 4 Hz). ^{13}C NMR (100 MHz, $CDCl_3$): δ 169.48, 147.27 (m), 146.33 (m), 144.79 (m), 143.94 (m), 117.21, 105.95 (m), 64.41, 32.05, 31.87, 27.47, 22.47, 13.99. ^{19}F NMR (100 MHz, $CDCl_3$): δ 139.08 (m), 143.87 (m). MS for $C_{13}H_{14}F_4N_4ONa$ calc'd 341.11, found 341.0 $(M+Na)^+$.

Synthesis of 2-[4-[(1S)-1-[[(R)-tert-butylsulfinyl]amino]-1-cyclopentylethyl]triazol-1-yl]-*N*-[(2,3,5,6-tetrafluorophenyl)methyl]hexanamide (intermediate S-6; Scheme S2). To a solution of intermediate **S-5** (57 mg, 0.18 mmol) and *N*-[(2S)-2-cyclopentylbut-3-yn-2-yl]-2-methylpropane-2-sulfinamide (1) (**S-3**, 52 mg, 0.22 mmol) in dichloromethane (3.8 mL) and H_2O (2.5mL) was added 0.72 mL of $CuSO_4$ (0.3 M solution in H_2O, 0.22 mmol) and 0.56 mL of sodium ascorbate (1.0 M solution in H_2O, 0.56 mmol). The biphasic reaction mixture was stirred vigorously for 16 h at which point it was diluted with dichloromethane and washed with saturated aqueous $NaHCO_3$ and saturated aqueous NaCl. The organic extracts were dried over $MgSO_4$, filtered, and evaporated, and the crude material was purified using automated flash chromatography (12 g column, 50–75% EtOAc/hexanes) to obtain a pale green foam, which was taken up in $CHCl_3$ and washed with saturated NH_4OH to remove residual copper ions. The organic layer was once again dried over $MgSO_4$, filtered, and evaporated to obtain intermediate **S-6** (89 mg, 89%) as a white foam that was a 70:30 mixture of diastereomers at the α methine position. R_f 0.17 (50% EtOAc/hexanes). ^{1}H NMR (400 MHz, $CDCl_3$): δ 7.71 (s, 0.7H), 7.69 (s, 0.3H), 7.33 (br s, 0.3H), 7.25 (br m, 0.7H), 6.95 (m, 1H), 5.15 (dd, 0.3H, J = 4, 8 Hz), 5.09 (dd, 0.7H, J = 4, 8 Hz), 4.49 (m, 2H), 3.83 (s, 0.3H), 3.78 (s, 0.7H), 2.70 (m, 0.3H), 3.61 (m, 0.7H), 2.27 (m, 1H), 2.17 (m, 0.7H), 2.12 (m, 0.3H), 1.67 (m, 4H), 1.50 (s, 5H), 1.31 (m, 6H), 1.15 (s, 9H), 0.82 (t, 3H, J = 8 Hz). ^{13}C NMR (100 MHz, $CDCl_3$): δ 168.67, 168.66, 154.05, 147.15 (m), 146.45 (m), 144.64 (m), 143.96 (m), 122.19, 120.91, 117.26 (m), 105.50 (m), 64.84, 64.46, 58.62, 58.33, 56.22, 50.42, 50.10, 32.33, 32.25, 28.17, 28.10, 27.43, 27.39, 27.36, 27.27, 26.20, 26.16, 26.06, 23.28, 22.77, 22.75, 22.41, 22.16, 22.13, 13.91. ^{19}F NMR (100 MHz, $CDCl_3$): δ 139.64 (m), 143.69 (m). MS for $C_{26}H_{37}F_4N_5O_2$ calc'd 559.26, found 560.2 $(M+H)^+$.

Synthesis of 2-[4-[(1S)-1-amino-1-cyclopentylethyl]triazol-1-yl]-*N*-[(2,3,5,6-tetrafluorophenyl)methyl]hexanamide hydrochloride (mML; Scheme S2). A solution of intermediate **S-6** (89 mg, 0.16 mmol) in HCl-dioxane (4.0 M, 0.40 mL, 1.6 mmol) was stirred for 3 h, at which point hexane (5 mL) was added. The solvent was evaporated, and then the resulting solid was titurated with hexanes, and then with Et_2O. The solid was collected, and the ether filtrate reserved, concentrated and purified by automated flash chromatography (4 g column, 10–15% $MeOH/CH_2Cl_2$) to afford the title compound as the free base. This material was treated with HCl-dioxane (1.0 mL), and further trituration as before afforded additional hydrochloride salt. The solids were combined and dried in vacuo to afford mML hydrochloride (70 mg, 90%), which was a 70:30 mixture of diastereomers at the α methine position. ^{1}H NMR (400 MHz, $CDCl_3$): δ 9.07 (s, 3H), 8.26 (s, 0.3H), 8.20 (s, 0.7H), 8.11 (s, 1H), 6.99 (m, 1H), 5.58 (br s, 0.3H), 5.48 (br s, 0.7H), 4.6 (m, 1.4H), 4.49 (m, 0.6H), 2.57 (m, 1H), 2.17 (br s, 1H), 2.06 (br s, 1H), 1.8–1.5 (m, 11H), 1.25–1.13 (m, 4H), 0.80 (t, 3H, J = 4 Hz). ^{13}C NMR (100 MHz, $CDCl_3$): δ 168.97, 148.34, 147.18 (m), 146.28 (m), 144.69 (m), 143.80 (m), 121.65, 116.91 (m), 105.82 (m), 64.27, 58.65, 58.40, 49.03, 32.55, 32.17, 27.70, 27.60, 27.50, 25.76, 25.60, 23.99, 22.08, 13.79. ^{19}F NMR (100 MHz, $CDCl_3$): δ 139.31 (m), 143.77 (shoulder, m) 143.93 (m). LRMS for $C_{22}H_{29}F_4N_5O$ calc'd 455.23, found 456.1 $(M+H)^+$.

Synthesis of 2-[(3R)-3-[3-oxo-3-[3-(2-oxopyrrolidin-1-yl)propylamino]propyl]spiro[1,2,4-trioxolane-5,2′-adamantane]-3-yl]ethyl *N*-[(1S)-1-cyclopentyl-1-[1-[1-oxo-1-[(2,3,5,6-tetrafluorophenyl)methylamino]hexan-2-yl]triazol-4-yl]ethyl]carbamate (TRX-mML; Scheme S2). To a solution of mML (HCl salt, 58 mg, 0.118 mmol) in DMF (1.0 mL) was added DIEA (57 μL, 0.33 mmol). The solution was stirred for 20 min, and then a solution of intermediate **S-1** (89 mg, 0.148 mmol) in DMF (1.0 mL) was added, followed by DMAP (3 mg, 0.02 mmol). The yellow solution was stirred for 22 h and then diluted with EtOAc. The organic layer was washed with saturated aqueous $NaHCO_3$ thrice and 1.0 M aqueous NaOH, and then saturated aqueous NaCl. The organic layer was dried over $MgSO_4$, filtered, and evaporated, and the crude material was purified using automated flash chromatography (40 g SiO_2, 5–10% MeOH/EtOAc) followed by preparatory TLC to obtain TRX-mML (40 mg, 37%) as a white foam. ^{1}H NMR (400 MHz, $CDCl_3$): δ 7.78 (br s, 1H), 7.64 (s, 1H), 7.22 (br s, 1H), 7.02 (m, 1H), 5.65 (br s, 2H), 5.21 (m, 1H), 4.54 (s, 2H), 4.18 (m, 1H), 4.05 (m, 1H), 3.39 (t, 2H, J = 8 Hz), 3.30 (m, 2H), 3.09 (m, 1H), 2.5–1.17 (m, 42H), 0.85 (t, 3H, J = 8 Hz). ^{13}C NMR (75 MHz, $CDCl_3$): δ 175.66, 172.41, 168.32, 120.97, 116.91, 112.16, 109.70, 105.54 (m), 61.18, 60.29, 56.06, 47.40, 40.19, 36.70, 36.33, 36.25, 36.16, 35.05, 34.80, 34.69, 34.58, 32.51, 31.92, 31.34, 31.02, 27.75, 27.14, 27.07, 26.78, 26.67, 26.40, 25.68, 25.57, 21.97, 17.92, 13.77. ^{19}F NMR (100 MHz, $CDCl_3$): δ 139.30 (m), 143.80 (m). MS for $C_{46}H_{63}F_4N_7O_8$ calc'd 917.47, found 918.4 $(M+H)^+$.

Synthesis of 2-[(4S)-spiro[1,3-dioxolane-2,2′-adamantane]-4-yl]ethanol (intermediate S-7; Scheme S3). A solution of adamantan-2-one (1g, 6.66 mmol) in toluene (18 mL) was treated with 1,2,4-butane-1,2,4-triol and a catalytic amount of camphor sulfonic acid (77 mg, 0.33 mmol). The reaction solution was refluxed for 2 d in a Dean–Stark apparatus. The solution was cooled and washed with water (2 × 10 mL), saturated aqueous $NaHCO_3$ (2 × 10 mL), and brine. The organic phase was dried over sodium sulfate and filtered, and concentrated crude material was purifed via automated flash chromatography to afford intermediate **S-7** (454 mg, 29%): ^{1}H NMR (400 MHz, $CDCl_3$) δ 4.26 (quin., J = 6.4 Hz,

1H), 4.07 (dd, J = 8.0, 6.1 Hz, 1H), 3.80–3.82 (m, 2H), 3.58 (t, J = 7.7 Hz, 1H), 2.52–2.55 (m, 1H), 1.66–1.98 (m, 16H); ^{13}C NMR (100 MHz, $CDCl_3$) δ 112.4, 75.3, 69.2, 31.2, 38.0, 37.2, 36.5, 35.8, 35.2, 35.1, 35.0, 34.7, 27.0, 27.0; MS calculated for $C_{14}H_{22}O_3$ 238.16, found (M+H$^+$) 239.03.

Synthesis of (4-nitrophenyl) 2-[(4R)-spiro[1,3-dioxolane-2,2′-adamantane]-4-yl]ethyl carbonate (intermediate S-8; Scheme S3). To a solution of intermediate **S-7** (200 mg, 0.84 mmol) in dichloromethane (2.8 mL) was added triethylamine (0.23 mL, 1.68 mmol) and *p*-nitrochloroformate (339 mg, 1.68). The reaction mixture was stirred overnight and then diluted with dichloromethane (15 mL) and washed with saturated aqueous $NaHCO_3$ (2 × 10 mL), water, and saturated aqueous NaCl. The organic layer was dried over sodium sulfate, filtered, and concentrated. The crude residue obtained was purified using automated flash chromatography (8% EtOAc/hexanes) to afford intermediate **S-8** (180 mg, 0.45 mmol, 53%): ^{1}H NMR (400 MHz, $CDCl_3$) δ 8.27 (d, J = 8.8 Hz, 2H), 7.38 (d, J = 9.0 Hz, 2H), 4.45 (m, 2H), 4.25 (t, J = 6.3 Hz, 1H), 4.11 (m, 1H), 3.62 (t, J = 7.2 Hz, 1H), 1.67–2.02 (m, 16H); ^{13}C NMR (100 MHz, $CDCl_3$) δ 155.7, 152.5, 145.5, 125.4, 121.9, 112.4, 72.3, 69.0, 66.8, 38.2, 37.2, 36.5, 35.2, 35.0, 34.9, 34.8, 33.3, 27.1, 27.0; MS calculated for $C_{21}H_{25}NO_7$ 403.16, found (M+H$^+$) 404.11.

Synthesis of 2-[(4S)-4-[3-oxo-3-[3-(2-oxopyrrolidin-1-yl)propylamino]propyl]spiro[1,3-dioxolane-2,2′-adamantane]-4-yl]ethyl *N*-[(1S)-1-cyclopentyl-1-[1-[2-oxo-1-(2,3,5,6-tetrafluorophenoxy)heptan-3-yl]triazol-4-yl]ethyl]carbamate (DXL-ML; Scheme S3). To a solution of intermediate **S-8** (25 mg, 0.063 mmol) in DMF (1 mL) was added ML (30 mg, 0.053 mmol) and DIEA (0.1 mL, 0.02 mmol). The reaction was stirred overnight, and then a single crystal of DMAP and an additional 1 equivalent of DIEA were added. The reaction mixture was stirred for an additional 2 d and then diluted with EtOAc (15 mL). The organic phase was washed with saturated aqueous $NaHCO_3$ (3 × 10 mL), water, saturated aqueous NaCl, and brine, and dried over sodium sulfate. The solution was filtered and concentrated, and the crude residue was purified using automated flash chromatography (5–25% EtOAc/hexanes) to afford DXL-ML (19.3 mg, 0.027 mmol, 51%): ^{1}H NMR (400 MHz, $CDCl_3$) δ 7.55 (s, 1H), 6.79–6.84 (m, 1H), 5.49–5.58 (m, 1H), 4.86 (m, 2H), 4.04–4.13 (m, 4H), 3.53–3.56 (m, 1H), 0.86–2.29 (m, 38H); ^{13}C NMR (100 MHz, $CDCl_3$) δ 199.4, 154.8, 152.3, 147.7, 147.7, 145.3, 145.2, 145.1, 141.8, 141.6, 139.2, 121.2, 111.9, 100.6, 100.4, 100.2, 77.4, 75.5, 72.9, 69.2, 65.6, 61.7, 56.3, 38.1, 37.3, 36.6, 35.2, 35.0, 35.0, 34.8, 33.7, 30.9, 29.8, 27.8, 27.8, 24.5, 27.4, 27.3, 27.1, 27.0, 25.9, 25.8, 25.7, 23.0, 22.0, 13.8; MS calculated for $C_{37}H_{48}F_4N_4O_6$ 720.35, found (M+H$^+$) 721.23.

1. Deu E, et al. (2010) Functional studies of Plasmodium falciparum dipeptidyl aminopeptidase I using small molecule inhibitors and active site probes. *Chem Biol* 17(8):808–819.
2. Deu E, Yang Z, Wang F, Klemba M, Bogyo M (2010) Use of activity-based probes to develop high throughput screening assays that can be performed in complex cell extracts. *PLoS ONE* 5(8):e11985.
3. Mahajan SS, et al. (2011) A fragmenting hybrid approach for targeted delivery of multiple therapeutic agents to the malaria parasite. *ChemMedChem* 6(3):415–419.
4. Brak K, et al. (2010) Nonpeptidic tetrafluorophenoxymethyl ketone cruzain inhibitors as promising new leads for Chagas disease chemotherapy. *J Med Chem* 53(4): 1763–1773.

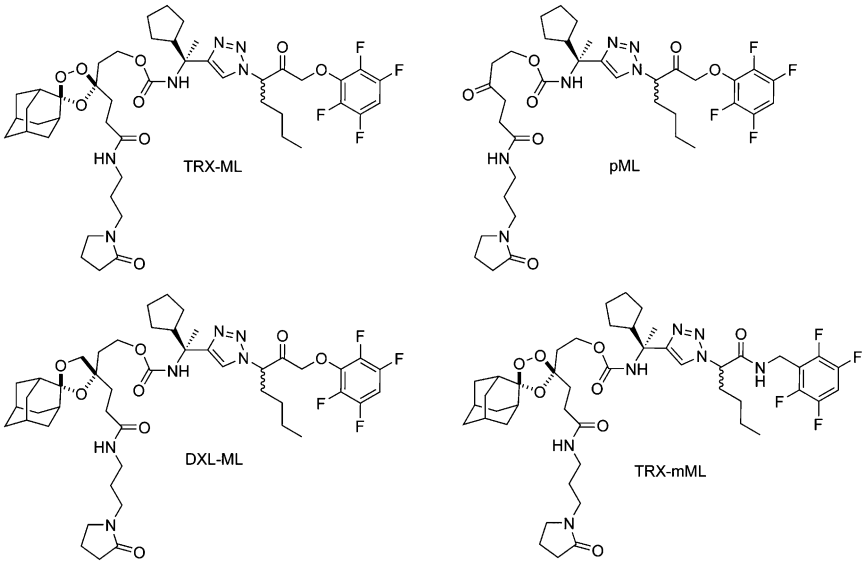

Fig. S1. Chemical structures of TRX-ML, DXL-ML, pML, and TRX-mML. Complete chemical structures of test compounds and controls. DXL-ML is a non-peroxidic, dioxolane analog of TRX-ML. The ketone pML is the intermediate formed following activation of TRX-ML by Fe^{II}, before elimination of free ML. TRX-mML is a close structural analog of TRX-ML bearing the inactivated (mock) DPAP1 inhibitor mML.

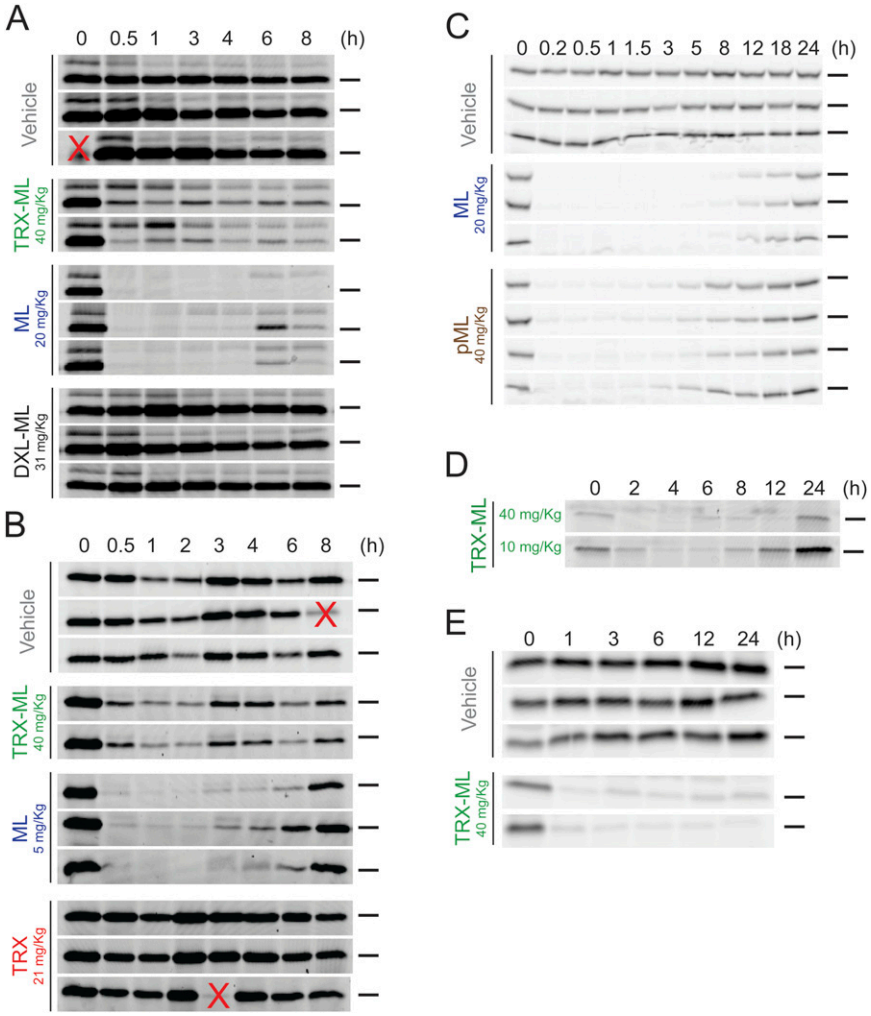

Fig. S2. Time course of DPAP1 inhibition in vivo. *A–E* correspond to different biological replicates. Infected mice at 20–40% parasitemia were treated with the indicated amount of compound. At different time points after treatment, 10 μL of infected blood was taken from the tail vein of the mice, and the residual DPAP1 activity was labeled with FY01. Bars indicate the location of DPAP1 in the gel. Note that, in *B*, there is a significant variation in the efficiency of DPAP1 labeling. During the course of this specific experiment, we made two stocks of 2 μM FY01 in PBS containing 2× heparin. One was used to label DPAP1 within the first 2 h of the time course, and the other between 3 and 8 h after treatment. The lack of stability of the probe under these conditions explains why labeling increased between the 2 and 3 h time points, and why the labeling efficiency decreased between 0 and 2 h and between 3 and 8 h in vehicle or control-treated mice. Because these labeling variations were systematic, they could be taken into account after normalization of the level of DPAP1 activity (*Materials and Methods*). Red crosses represent experimental errors and were not included in the quantification of DPAP1 labeling shown in Fig. 5*C*.

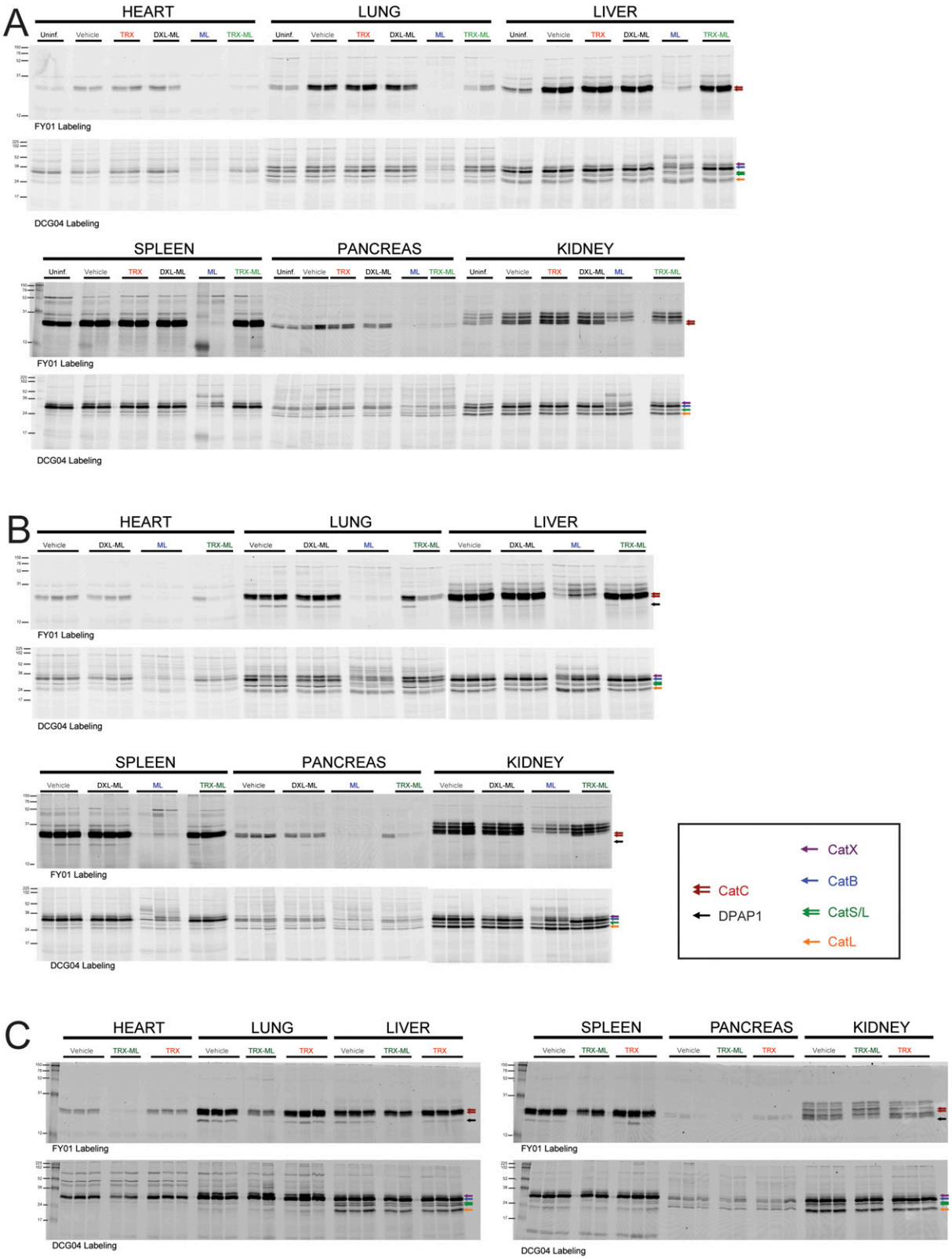

Fig. S3. Measurement of host cathepsins inhibition. Each panel represents a different experiment. *Plasmodium berghei*-infected mice at 1–3% *(A)* or 20–40% *(B* and *C)* parasitemia were treated with vehicle, TRX (31 mg/kg), DXL-ML (20 mg/kg), ML (20 mg/kg), or TRX-ML (40 mg/kg). After 8 h, mice were euthanized and perfused, and the indicated organs were collected and frozen in liquid nitrogen. After lysis, the soluble fraction of each organ was reacted with a combination of FY01 and DCG04 (1 μM of each) for 1 h and run on an SDS/PAGE gel. Labeled proteins were visualized by scanning the in-gel fluorescence. Differently colored arrows indicate each of the labeled cathepsins (CatC, X, B, S, and L). In some instances, we were able to see a band corresponding to DPAP1 in organs collected from mice that were treated at high parasitemia. The presence of parasite protein in mouse tissue is likely due to inefficient perfusion of these specific mice. For comparison purposes, the level of cysteine cathepsin activity in two uninfected and untreated mice (Uninf.) was also measured. Quantification of the labeling of each protease is shown in Fig. 6 and Figs. S5 and S6.

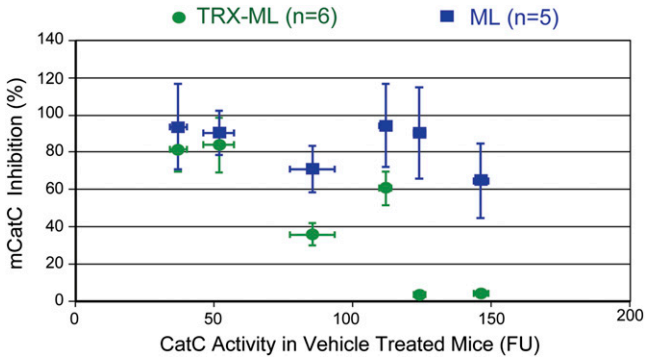

Fig. S4. Inverse correlation between the endogenous levels of CatC activity in different organs and the level of CatC inhibition in mice treated with TRX-ML ($n = 6$) and ML ($n = 5$). Because no significant differences were observed between mice treated at low (Fig. 6*B*) or high (Fig. 6*C*) parasitemia, average values were obtained by combining the data of the two experiments.

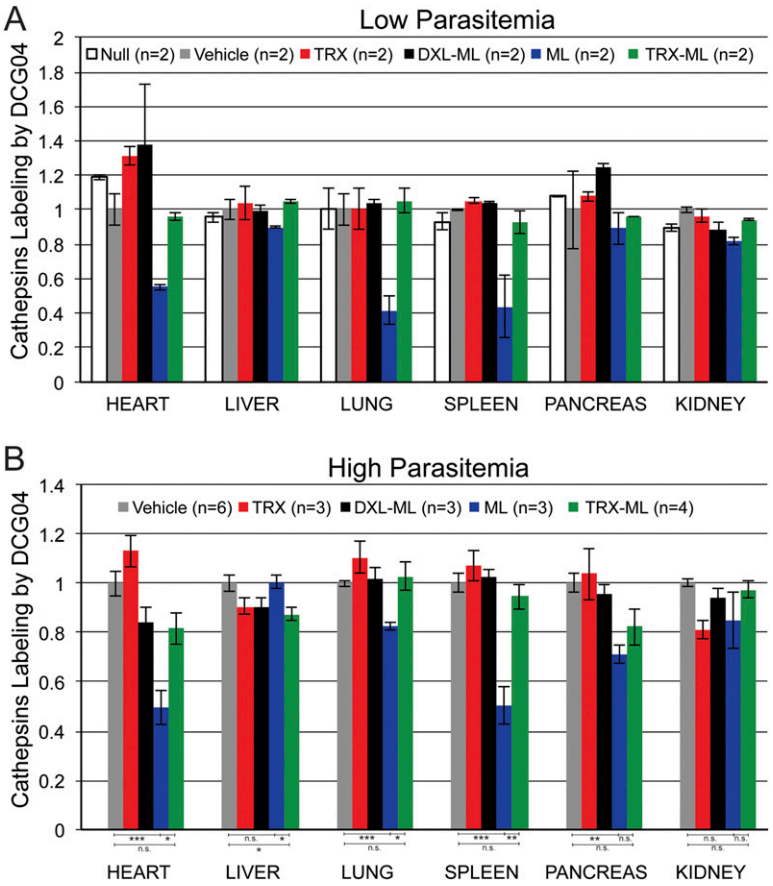

Fig. S5. Global quantification of host off-target effects. The global level of cysteine cathepsin activity measured by DCG04 was quantified from the gels shown in Fig. S3 using ImageJ. *A* and *B* correspond to data obtained from mice treated at low or high parasitemia, respectively. The number of mice treated with each compound is shown in parentheses. Bars represent SEs and *t* test significance values are shown (*$P < 0.05$; **$P < 0.01$; ***$P < 0.001$; n.s., not significant).

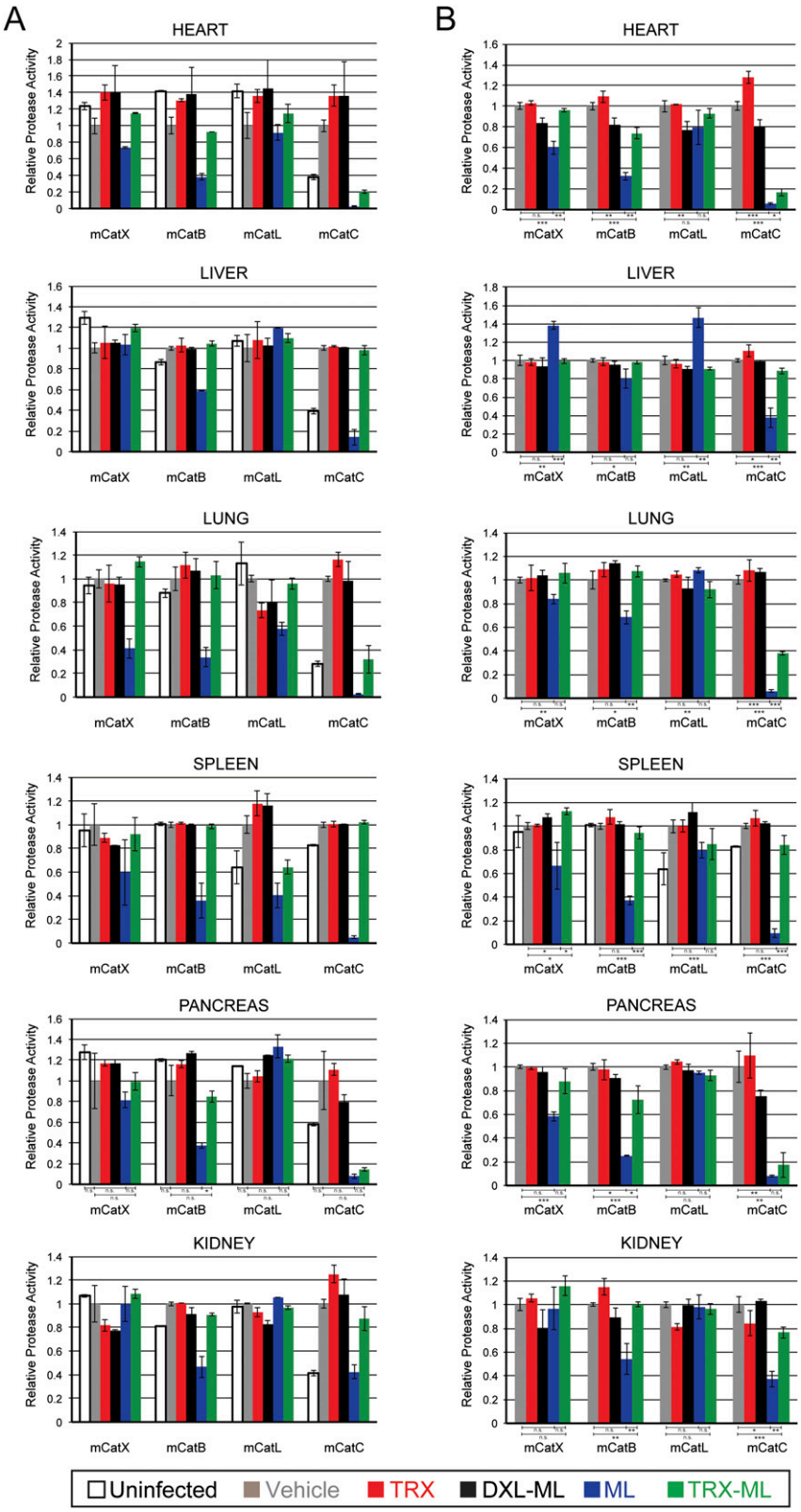

Fig. S6. Quantification of individual host cathepsin inhibition. The activity level of each cysteine cathepsin labeled by DCG04 (CatX, B, and L) and FY01 (CatC) was quantified from the gels shown in Fig. S3 using ImageJ. *A* and *B* correspond to data obtained from mice treated at low or high parasitemia, respectively. The number of mice treated with each compound is shown in Fig. S5. Bars represent SEs, and *t* test significance values are shown (*$P < 0.05$; **$P < 0.01$; ***$P < 0.001$; n.s., not significant).

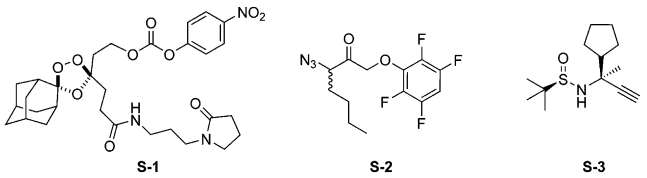

Fig. S7. Key synthetic intermediates. Synthetic intermediates **S-1**, **S-2**, and **S-3** were used in the preparation of final test compounds and controls.

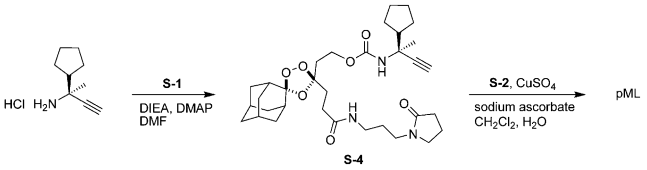

Scheme S1. Synthesis of pML. Synthetic route used to prepare pML. In the second step, the trioxolane ring is hydrolyzed under the conditions of the copper promoted [3+2] cycloaddition, yielding the ketone pML.

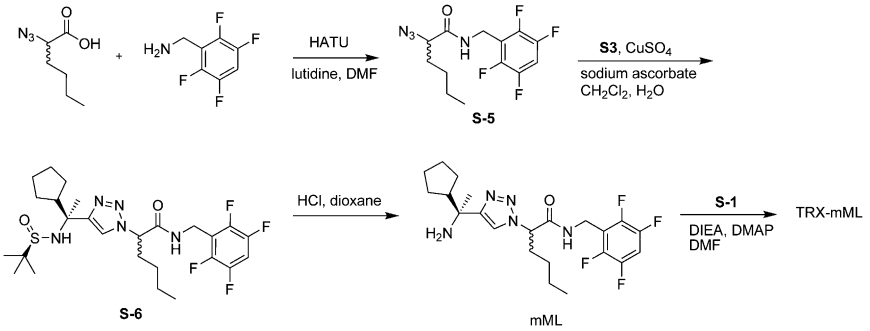

Scheme S2. Synthesis of mML and TRX-mML. Synthetic route used to prepare the mock form of ML, denoted mML, and its trioxolane conjugate TRX-mML.

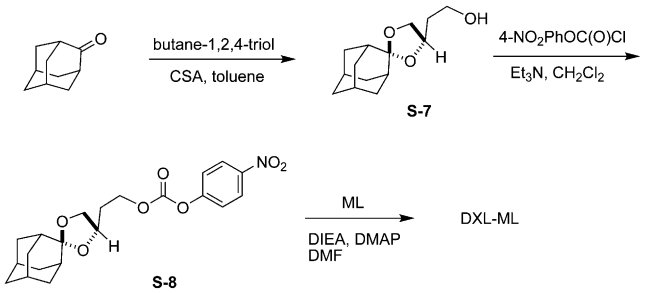

Scheme S3. Synthesis of DXL-ML. Synthetic route used to prepare the nonperoxidic dioxolane control DXL-ML.